Two step sintering process and metal grid design optimization for highly efficient ITO free organic photovoltaics

Marios Neophytou [a], Efthymios Georgiou [a], Marios M. Fyrillas [b], Stelios A. Choulis [a,*]

[a] Cyprus University of Technology, Molecular Electronics and Photonics Research Unit, 45 Kitiou Kyprianou St., 3041, Limassol, Cyprus
[b] Frederick University, Department of Mechanical Engineering, 1303 Nicosia, Cyprus

ABSTRACT

The need for inexpensive alternative to indium doped tin oxide (ITO) transparent electrodes is imminent for cost-efficient solution processed optoelectronic applications. ITO-free transparent electrodes can be based on inkjet-printed Silver (Ag) nanoparticles grids embedded into PEDOT:PSS buffer layers. We present an in-depth investigation of the morphological evolution of the inkjet printed Ag nanoparticle sintering process combined with an ultimate control of the printed grid design requirements for efficient ITO-free organic photovoltaics (OPVs). We report on glass/ITO-free P3HT:$PC_{60}BM$ and Si-PCPDTBT:$PC_{70}BM$ based OPVs with power conversion efficiency of 2.8% and 4.9% respectively. These devices exhibited minimal losses when compared to reference ITO-based OPVs.

1. Introduction

The need for cheap, thinner and lighter electronics is increasing due to the rising demand for applications within the fields of life sciences and engineering. For this reason organic optoelectronic devices have been attracting growing scientific interest during the last decade. Organic photovoltaic (OPV) commercialization is only feasible through printing technologies such as gravure, flexography and inkjet printing.[1] The latter with a drop-on-demand (DOD) technology allows the user to pre determine the coordinates of each droplet deposition on the substrate, to control droplet formation, minimizing material loss and to reduce if not eliminate the need for post-production treatment [2,3].

Most efficient reported organic solar cell devices are based on the so-called bulk heterojunction (BHJ) architecture, where a mixture of conjugated polymers and soluble fullerene derivatives constitute the semiconducting photoactive layer. Recent progress in BHJ OPVs includes power conversion efficiencies (PCE) of more than 9% using new synthesized active layers materials [4], and improved stability under real time outdoor [5] and accelerated indoor lifetime performance testing [6]. Nevertheless, in order to challenge other solar energy harvesting thin film technologies, PCE, stability and fabrication cost must be further improved. The large majority of the devices reported in the literature are

fabricated in controlled environment (clean room) or inert atmosphere (glove box) and employ indium doped tin oxide (ITO) as the transparent electrode [7–9]. Despite the fact that ITO exhibits high electrical conductivity and light transmittance, cost intensive vacuum deposition and high temperature post treatment processes render it as the most expensive component of the organic electronic device structure [10,11]. Additionally, not only may the ITO price rise in the near future due to low indium reserves, but also the ITO/PEDOT:PSS interface has been found to be one of the degradation parameters affecting the device stability [12]. Furthermore, mechanical properties of ITO, such as high rigidity, are responsible for crack formation on the surface of the transparent oxide hindering efficient charge carrier collection [13].

Numerous research groups have developed alternative transparent conductive electrodes in an effort to efficiently replace ITO such as sputtered fluorine doped tin oxide (FTO) [14], thermally evaporated metal grids, single-walled carbon nanotubes (CNTs) [15] and monoatomic graphene layers [16]. Even though in some cases transmittance and conductivity similar to ITO have been achieved, the employed vacuum techniques are not compatible with roll-to-roll production [17], CNTs are expensive and toxic [18] and manufacturing graphene on a commercial scale is still challengingwhen it comes to large scale manufacturing [19]. PEDOT:PSS is considered to be another promising candidate for ITO-free OPV devices. The latter when deposited in thin films, although it exhibits high transmittance, has a high sheet resistance (R_{SH}). In principle, R_{SH} may obstruct collection and extraction of

* Corresponding author. Tel.: +357 25002605.
 E-mail address: stelios.choulis@cut.ac.cy (S.A. Choulis).

the photogenerated charged carriers resulting in devices with limited overall performance. To address this problem, inkjet printed silver nanoparticle (Ag NP) current collecting grid lines have been integrated with PEDOT:PSS. Metal grid lines for photo-generated charge collection have been widely used for inorganic solar cells; Tom Aernouts introduced similar concepts in OPVs [20]. Since then, plethora of scientific publications have been reported. Tvingstedt et al. fabricated Ag grid lines by employing structured polydimethylsiloxane (PDMS) molds that resulted in power conversion efficiency of 1% [21]. Thereafter Kang et al. suggested that electrical conductivity can be increased by depositing thicker metal grid lines. Devices fabricated with different novel metal grids resulted in PCEs of 2% [22]. More recent, Galagan et al. reported inkjet printed Ag grids combined with PEDOT:PSS forming solution processed transparent electrode. For the aforementioned device architecture, with flexible and glass substrates, PCEs of 1.5% were achieved. The same group reported sheet resistance values as low as 1 Ω/□ by embedding thick Ag-grid lines in the barrier foil [23,24].

In our previous work, two different types of low cost PEDOT:PSS derivatives were utilized[25]. Four printed grid lines were employed providing optical transmittance higher than 90% throughout the visible spectrum and reproducible glass/ITO-free OPV devices with PCE of 1.96%. At the same time ITO-based devices exhibited PCE of 3%. Sintering process was performed at 140C for 20 min. With this process spikes of a few tens of nanometers higher than the overall line height were formed, increasing leakage current, thus limiting device performance. Additionally, devices were suffering to some extent from delamination upon PEDOT:PSS deposition.

In continuation of this work we hereby report an in depth investigation of the inkjet printed Ag nanoparticle morphological evolution through different sintering processes. Upon thermal elevation in single step sintering, the sheet resistance of the metal grids was reduced, reaching values as low as 22.7Ω/□ at high temperatures. Importantly, when a two-step process is applied, combining low and high temperature, R_{SH} values similar to that of ITO (8.5 Ω/□) were obtained. With this two-step sintering process we gained absolute control over the internal flows governing line formation and diminished printed line delamination. Furthermore we present a detail analysis and correlation of PCE device performance relevant to metal-grid design configuration. This allowed us to optimize the number of current collecting grid lines and achieve better overall device performance. Based on the above mentioned improvements we report 30% further increase of the PCE to 2.82% while achieving 47% fill factor (FF), 10.4 mA/cm² short circuit current density (Jsc), 0.57 V open circuit voltage (Voc) with P3HT:PCBM based ITO-free devices. The same experimental procedure for the optimized transparent electrode was also applied with high performance Si-PCPDTBT:PC₇₀BM system resulting in PCE of 4.9%. For both systems, we report ITO-free PCE values similar to that of ITO. This strongly suggests that Ag NP grid lines/ PEDOT:PSS transparent electrode configuration is a viable and competitive candidate to replace ITO.

2. Materials and methods

Silver nanoparticle ink (SunTronic Jet Silver U5603) was inkjet printed using a Fujifilm DMP 2800 series printer on top of glass substrates. The print head was set at 700 μm above the substrate using a drop spacing of 35 μm and a substrate temperature set at 35 °C. On top of the sintered current collecting grid lines diluted PEDOT:PSS (Clevios PH) with isopropyl alcohol in a 1:3.2 ratio was doctor bladed. Residual solvent was removed by thermally annealing the layers at 140 °C for 30 min. Afterwards, P3HT and PCBM, purchased from Rieke Metals Inc and Solene BV respectively, were blended together in a 1:1 ratio forming the optically active layer. Solutions were left stirring separately overnight on a hotplate at 65 °C. After mixing, P3HT:PCBM solution was doctor bladed on top of PEDOT:PSS layer with blading speed of 20 mm/s [25]. Following thermal evaporation of 100 nm of aluminum, devices were annealed on a hotplate in ambient conditions for 22 min at 140 °C. For the Si-PCPDTBT: PC₇₀BM devices, solution was diluted separately overnight in o-DCB in a 1:1.5 ratio. Active area for the OPV devices presented is 9 mm². Each layer thickness was measured with a Dektak profilometer and morphological studies were performed with a Nanosurf easyscan 2 atomic force microscopy instrument in a tapping mode. A four-point-probe (Jandel RM3000) conductivity meter was employed for the determination of the sheet resistance. J/V characteristics were measured with a Keithley 2420 source meter under 100 mW/cm² (A.M. 1.5 G) employing a Newport solar simulator. The Xe lamp was calibrated with a Newport Si photodetector.

3. Results and discussion

Scheme 1a shows Ag NP ink before and after sintering the droplet shape. The latter severely varies depending on the sintering processing conditions. Inkjet printed Ag NP droplets are governed by two "gastronomical" effects: the coffee-ring and tears-of-wine effects. Around fifteen years ago Robert Deegan explained the so-called coffee-ring effect [26]. It was suggested that mainly due to capillary effect a flow of liquid is produced in a drying droplet due to uneven and inconsistent evaporation rate of
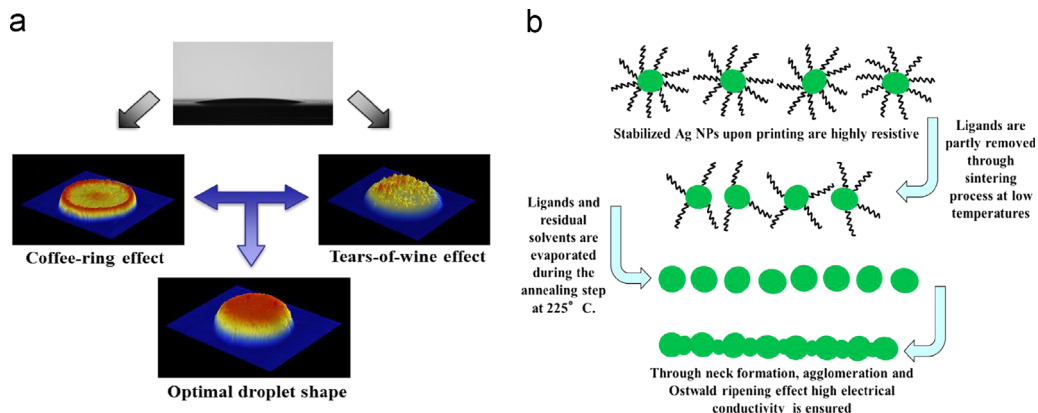
Scheme 1. (a) Capillary and Marangoni flows affect final line shape of the inkjet printed Ag nanoparticles. (b) A schematic illustration of the proposed two-step sintering process of inkjet printed Ag nanoparticle grid lines.

the solvent. The latter is more intense at the edges of the droplet resulting in replenishing the evaporated solvent from the center. This creates only an internal flow that potentially can transfer all solute to the contact line, forming high perimeter concentration of solutes. On the contrary, due to Marangoni flow, the tears-of-wine effect tends to redistribute the solute to the center of the droplet [27]. The solvent mixture that is used for the Ag nanoparticle dispersion consists of ethanol and ethylene glycol with surface tensions at 20 °C of ∼22 mN/m and∼48 mN/m, respectively [28]. Evaporation of ethanol (lower boiling point and surface tension) occurs everywhere along the droplet-air interface. This results in a concentration reduction of ethanol at the interface when compared to the bulk of the droplet. As a result, an immediate rise in surface tension is expected due to the higher concentration of ethylene glycol. This leads to an increase in the surface tension along the vertical direction with higher surface tension at higher regions, forming an upward flow towards the droplet-air interface as schematically depicted in Scheme 1a.

Capillary flow, as one of the dominant flows in inkjet printed Ag NP line formation, results in moderate overall height lines with increased line width. At extreme cases capillary flow may push most of the solute to the edges of the droplet resulting in spike formation and M-like line shape. Depending on how pronounced this formation is, spikes can penetrate the PEDOT:PSS hole selective contact and/or the optically active layer resulting in OPV devices with high leakage current or shunt ratio [25,29]. On the other hand, Marangoni flow will result in completely different line shape. Here, heights of the droplet may potentially reach the μm scale with smaller widths compared to the coffee-ring effect. Spike formation is also likely to occur, depending on the intensity of the flow, but in this case at the center of the droplet, as schematically shown in Scheme 1a.

In order to maximize the number of photons reaching the organic semiconductor, the device effective area coverage by the metal grid line must be kept as low as possible when at the same time electric conductivity remains at high values. Furthermore, in an effort to avoid shunts in the device and ensure efficient carrier collection selectivity, printed grid lines should be completely covered with PEDOT:PSS which can be detrimental for light absorption. A fine balance of the effect of these predominant flows must be achieved, thus, attaining optimal printed grid line shape with moderate height and narrow width is desired (Scheme 1a).

A Dimatix 2800 material inkjet printer with 10 pL cartridges was utilized to deposit the Ag nanoparticle grid lines on glass substrates. After printing, samples were placed on a hotplate in ambient conditions for sintering. In an effort to gain control on the final grid line formation various sintering temperatures, ranging from 5 °C to 225 °C, were applied. For 5 °C sintering temperature, samples were stored in a common refrigerator and were visually inspected until mirror-like appearance occurred. Afterwards, four-point probe measurements were performed in order to determine sheet resistance values of the printed Ag NP current collecting grids. As illustrated in Fig. 1a, a clear downward trend of obtained sheet resistance values is revealed. Upon temperature elevation during the sintering process R_{SH} is significantly reduced by four orders of magnitude reaching values as low as 22.7 Ω/□ at 225 °C.

Aiming to further understand R_{SH} relation to elevated sintering temperature, the morphology of the previously mentioned printed grids was investigated with atomic force microscopy (AFM). Fig. 1b shows representative morphological images of Ag NP grid lines sintered at different temperatures. When sintering was performed at 35 °C, a relatively smooth surface was observed with nanoparticle size being evenly distributed over the scanned area. Once the temperature was increased to 65 °C, domains with slightly larger nanoparticle size emerged. This is also observed when sintering

temperature was elevated to 140 °C. A steady transferal of the nanoparticle size distribution towards larger values is observed. The latter is justified and complimented through AFM characterization (Fig. 1b), where high sintering temperature led to clusters cores formation with sizes larger than 300 nm. In some cases these printed Ag NP lines exhibited deep surface cracks due to brisk solvent removal, suggesting potential failure in current collection.

In theory, metal nanoparticles have considerably high surface area/volume ratio due to their size. In addition, molecules on the surface of the nanoparticles are relatively energetically unstable when compared to those within the bulk. When this happens, surface atoms migrate in the solution and nanoparticles shrink over time. As a consequence, when the metal atom concentration becomes saturated, they will all merge into forming larger particles. This phenomenon is called Ostwald ripening [30].

As previously mentioned, inkjet printed Ag nanoparticle grid lines with high height and surface roughness could negatively affect the overall performance of OPV devices. Although R_{SH} of 22.7 Ω/□ has been obtained, morphological disadvantages outmatch that. In an effort to achieve grid lines with minimized sheet resistance and matching values obtained with sputtered ITO, further experiments were performed. In Fig. 1c, sheet resistance values in respect to sintering time are shown. Printed grid lines were exposed at 65 °C for 60, 120 and 720 min. The specific temperature was chosen as it could provide the desired printed grid line profile, as previously discussed (Scheme 1a). A fine control of the dominating internal flows was achieved through careful avoidance of undesirable line formations. Each grid line had 45–50 μm width and ∼200 nm uniform height. At 65 °C and 1 h of exposure 2900 Ω/□ were obtained. While at the same time, samples that were heated up for 120 min, provided values one order of magnitude lower. When samples were left on a heated hotplate overnight for 12 h, sheet resistance was further reduced to 427 Ω/□, (Fig. 1c). The reduction of almost a factor of 7 in obtained R_{SH} values is attributed to the slowly evaporated solvent mixture of the Ag nanoparticle dispersion, suggesting gradual nanoparticle agglomeration. At 65 °C ethanol is primarily evaporated as it has a boiling point of 78.4 °C with the remaining ethylene glycol (boiling point 197 °C) prohibiting further R_{SH} reduction. Regardless of the latter, all samples sintered at 65 °C, remarkably result in optimum line shape, which suffer from severe delamination upon water-based PEDOT:PSS deposition for OPV device fabrication. Residual ethylene glycol causes inability in nanoparticle adhesion on the substrate.

As electrode delamination is catastrophic for OPV device performance, an additional annealing step at higher temperature is introduced. As previously mentioned when samples were thermally annealed for 30 s at 225 °C, residual ethylene glycol was also evaporated from the printed grid lines. Importantly, this additional short annealing step assisted in further enhancing inkjet printed Ag nanoparticles grid lines sheet resistance, reporting values of 8.5 Ω/□. In Fig. 1c, it can also be seen that the longer the sintering time at 65 °C is, the lower the sheet resistance improvement upon further annealing at 225 °C for 30 s. This is explained by the fact that less ethylene glycol has remained within the Ag grid lines.

In an effort to identify the reason for diminishing R_{SH} values, AFM images were taken. Fig. 1d shows morphological evolution of printed grid lines sintered at 65 °C for different time and when the two-step sintering process concept described above was applied. When the grid lines were sintered for a longer period of time, the surface roughness increased by approximately 10 nm. Domains where nanoparticles are agglomerated are noticeable when observing the substrates being treated for 12 h due to gradual merging as stated above. Surface roughness is relatively more pronounced when annealing took place and average particle size has been
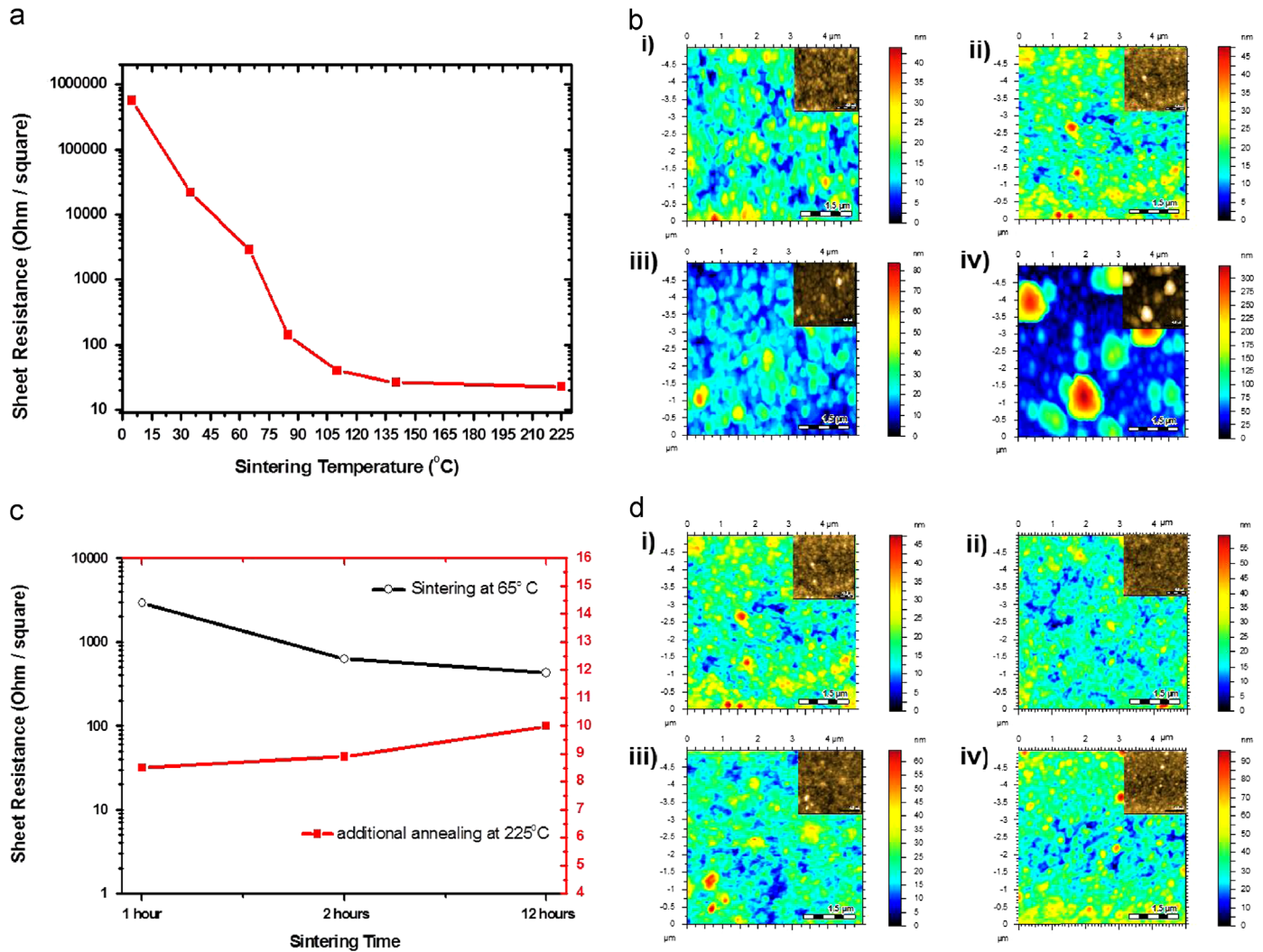
a

b

c

d

Fig. 1. (a) Sheet resistance relation to various sintering temperatures. (b) AFM images of inkjet printed Ag nanoparticle grid lines when sintered at (i) 35 °C, (ii) 65 °C, (iii) 140 °C and (iv) 225 °C. (c) Investigation of sheet resistance evolution when sintering at 65 °C for 1, 2 and 12 h (open black circles) and upon the addition of an annealing step at 225 °C for 30 s. (d) AFM images of the grid lines sintered at 65 °C for (i) 1 h, (ii) 2 h, (iii) 12 h and (iv) 1 h with short annealing.

almost doubled. Towards a better evaluation, OPV devices employing the suggested sintering methodology for inkjet printed Ag nanoparticle grid lines embedded into PEDOT:PSS (Heraeus Clevios PH) were fabricated and characterized. Through waveform modification printed lines exhibit an average width of 47 μm. The combination of line width and height reported in this paper is among the finest ever published in the literature for inkjet printed Ag nanoparticles [23,24,31,32]. The percentages of the OPV device active area that is covered with grid lines are shown in Table 1. On top of the current collecting line network, low cost PEDOT:PSS (Heraeus Clevios PH) was doctor bladed in ambient conditions. Prior to thermal deposition of an aluminum layer of 150 nm thickness, a mixture of P3HT:PCBM in a 1:1 ratio within chlorobenzene was doctor bladed as well as described in more details within the experimental section.

In order to establish a fine balance between efficient current collection and covered area percentage ratio, organic photovoltaic devices were fabricated with different number of printed Ag nanoparticle current collecting lines, ranging from 1 to 10. From illuminated current density versus applied voltage (J/V) characteristics (Fig. 2a) and Table 1 which summarizes the OPV performance values at A.M. 1.5G, 100 mW/cm^2 conditions, one can easily conclude that when the Ag nanoparticle grid line number is increased, improved FF values are obtained. Devices with 1 to

Table 1
Summary of the numerical data extracted from the illuminated J/V characteristics under 100 mW/cm^2 (A.M. 1.5G) obtained from ITO-free P3HT:PCBM based OPV devices employing different fraction of inkjet printed Ag nanoparticle current collecting grid lines.

Number of Ag NP grid lines	Covered area (%)	V_{OC} (V)	J_{SC} (mA/cm^2)	FF (%)	PCE (%)
1	1.6	0.52	4.59	29.7	0.71
2	3.2	0.55	5.89	31.6	1.04
3	4.8	0.57	6.23	35.1	1.27
5	7.9	0.56	9.28	42.2	2.19
8	12.7	0.56	10.6	47.9	2.82
10	15.8	0.57	9.35	49.2	2.64
Reference	–	0.54	10.1	54.1	2.95

3 grid lines, exhibit large regions where overall R_{SH} is mainly accredited to the PEDOT:PSS layer. The latter increases resistance losses within the device, demonstrating high series resistance (R_S) values as illustrated in the J/V characteristics at $+1$ V (see Fig. 2a). R_S losses are mainly the reason for the low FF values of the corresponding OPV devices with overall Ag grid-covered area from 1.6% to 4.8% (1 to 3 lines). Once the covered area was increased to 7.9–12.7% (5 and 8 lines respectively) FF and PCE values performance significantly improved (Fig. 2a). A higher percentage of the
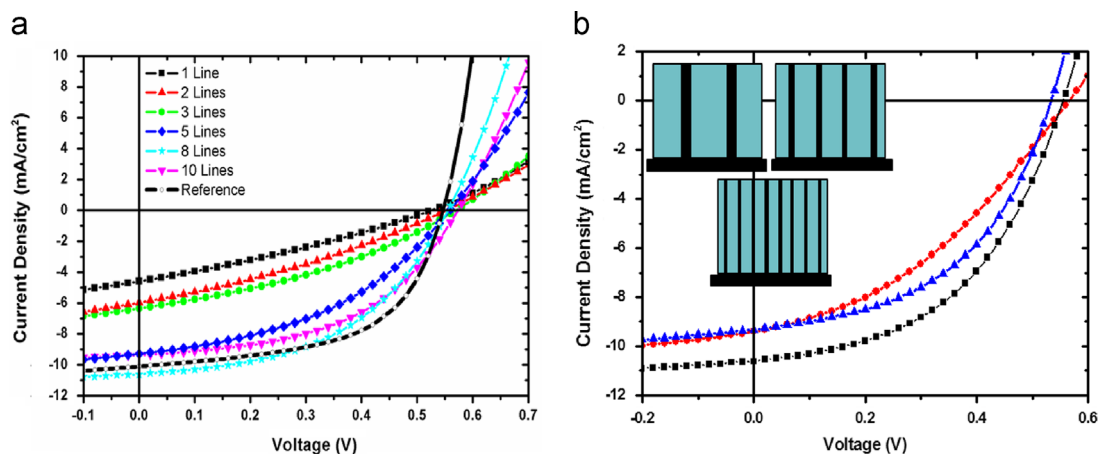
Fig. 2. (a) Current density versus applied voltage (J/V) characteristics under 100 mW/cm^2 (A.M. 1.5G) of ITO-free P3HT:PCBM based OPV devices which employ different number of current collecting grid lines. (b) J/V characteristics of different electrode architecture, 2 (━●━), 4 (━▲━) and 8 (━■━) lines, with the same overall active area covered with Ag nanoparticle grid lines. Electrode structures are schematically depicted in the inset.

Table 2
Summary of photovoltaic parameters of ITO-free P3HT:PCBM based OPV devices using inkjet printed Ag nanoparticle grids of various widths as the anode.

Number of Lines × line width (μm)	V_{OC} (V)	J_{SC} (mA/cm^2)	FF (%)	PCE (%)
2 × 182	0.56	9.4	37.7	2.0
4 × 92	0.53	9.3	48.4	2.4
8 × 47	0.56	10.6	47.9	2.82

photogenerated carriers were extracted and collected as indicated by the observed improvement of FF and J_{SC} values (Table 1). A turning point in grid line coverage was identified when the covered area reached value of 15.8% (10 lines). Incoming photons were reflected on the Ag nanoparticle grid lines forming shadow effects. This is echoed on reduced J_{SC} value when compared to those obtained at Ag grid-covered area of 12.7% (8 lines). Consequently, the optimum device architecture is recorded when the inkjet-printed Ag nanoparticles grids covered area was around 12.7% (8 lines) giving a PCE of 2.82% with V_{OC}, J_{SC} and FF values of 0.56 V, 10.6 mA/cm^2, 47.9% respectively (Fig. 2a and Table 1). In the same run ITO-based reference P3HT:PCBM devices were fabricated for comparison, delivering PCE, V_{OC}, J_{SC} and FF values of 2.95%, 0.54 V, 10.1 mA/cm^2 and 54.1% respectively.

As shown in Fig. 2b (inset), different metal-grids architecture organic solar cells with similar coverage area were fabricated aiming to further gain in device performance. Printed Ag NP grid lines were printed with increased horizontal distance from each other (pitch size). J/V characteristics of these devices are illustrated in Fig. 2b. At first, two lines of 182 μm width with increased pitch size deliver poor device performance as presented in Table 2 due to the fact that the increased pitch size results in locally increased sheet resistance. The latter exhibits increased recombination regions within the device active area, which significantly reduced charge collection properties. Furthermore, four lines of 92 μm width were employed as transparent electrode, presenting significantly improved FF values. These samples attest regions of different sheet resistance values, as some sections were dominated by high R_{SH} from PEDOT:PSS, and some others with high electrical conductivity from the Ag NP. This is attributed to the pitch size values of those samples. Charge collection occurs in the immediate vicinity of the four grid lines; however this area does not cover the entire active area, leaving some areas where charge collection cannot occur. This results in an under-performing ITO-free electrode. We conclude that thinner lines are essential to achieve
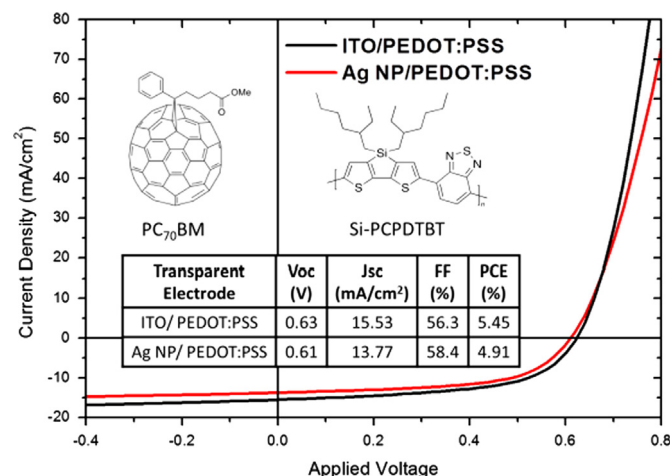

Fig. 3. Illuminated (100 mW/cm^2, A.M. 1.5 G) J/V characteristics for Si-PCPDTBT: PC$_{70}$BM based devices. Ag NP/ PEDOT:PSS (red line) transparent electrode was employed and compared with reference devices with ITO/ PEDOT:PSS (black line). Inset: the chemical structure of the used materials and table with both device parameters. (For interpretation of the references to color in this figure legend, the reader is referred to the web version of this article.)

evenly distributed charge collection across the entire active area. Based on the above processing conditions for optimized ITO-free OPVs, PCE in the range of 2.8% is repeatedly achieved. This series of experiments clarifies the need for even distribution of the electrical conductivity of the electrodes, ensuring uniform carrier extraction throughout the device active area.

Gained knowledge from the P3HT:PCBM OPV devices employing the optimized ITO-free electrodes was also applied to a higher PCE material system based on blends of Si-PCPDTBT:PC$_{70}$BM. Fig. 3 shows light J/V characteristics of Si-PCPDTBT:PC$_{70}$BM based OPVs using ITO/PEDOT:PSS and Ag NP/ PEDOT:PSS transparent anodes. The obtained PCEs were 5.4% and 4.9% respectively in excellent agreement with performance parameters behavior of the P3HT: PCBM based OPVs data presented in details above.

The corresponding ITO-free OPV devices for both materials systems under study exhibited slightly lower PCE values when compared to reference ITO-based OPV devices. To identify these losses Krebs et al. employs a Light Beam Induced Current (LBIC) technique that can assist in grid geometry and active area definition for optimized device performance [33]. In this study, a finite element simulation was employed. In principle, despite the fact
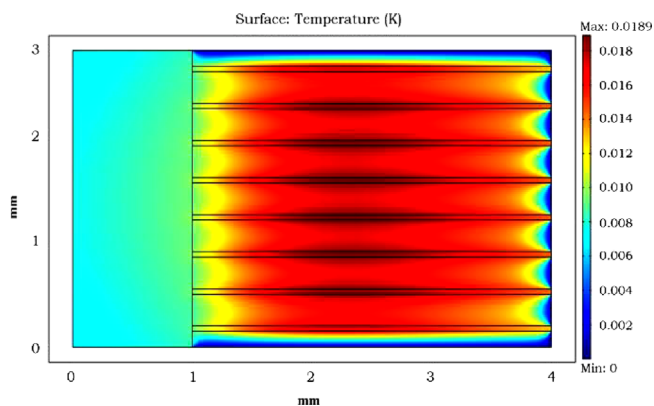
Fig. 4. The temperature distribution within the transparent electrode was simulated with zero temperature set as the ambient. Due to the small thickness of the Ag NP/PEDOT:PSS electrode ($\sim$210 nm) in comparison to the finished device overall thickness, it is assumed to be 2-D where natural convection is included as a heat sink in the governing equation. In addition, the model assumed that heat is generated in the silver current collecting grid lines due to the horizontal movement of the photogenerated carriers. The simulation was performed on COMSOL multiphysics.[34].

that high electrical conductivity of the Ag nanoparticle current collecting grids is achieved, the electrode still resists carrier flow. The interaction of Ag atoms with charge carriers can only result in resistive heating Fig. 4. shows the temperature distribution within the transparent electrode simulated with zero Celsius degree set as the ambient temperature using the COMSOL multiphysics software [34]. The finite element simulation indicates homogeneous heat distribution on the Ag NP/PEDOT:PSS surface, suggesting evenly dispersed photogenerated charge carrier extractionthus efficient electrode charge collection properties. At the edges of the proposed electrode configuration with 8 lines though, charge collection is under-performing, a factor that can be responsible for the minimal losses observed when ITO-free PCE values are compared with reference ITO-based OPVs.

We would like to highlight that the results reported are based on glass substrates/small active area. PCE reduction is expected for larger than 1 cm^2 active area devices due to series resistance (Rs) increase [35,36]. Devices fulfilling OPV product development targets [37,38] include flexible, large area, ITO and evaporation free OPV development. These challenges are not discussed in the current manuscript. The above parameters as well as device stability issues will be discussed in future publications.

4. Conclusions

In conclusion, various sintering temperatures were applied in an effort to achieve desired inkjet printed Ag nanoparticles current collecting grid line profile. AFM images were taken aiming to better understand obtained morphology. Despite the fact that smooth layers were achieved at lower sintering temperature, severe grid-line delamination was observed. Importantly, a fine balance of the line shape and morphology was achieved by introducing the two-step sintering process described in this paper. Samples were initially sintered at 65 °C for 1 h, followed by an additional 30 s processing annealing step at 225 °C. The proposed two-step sintering process resulted in R_{SH} values of 8.5Ω/$\Box$ and at the same time ensured that no residual solvent was trapped inside the printed grid causing catastrophic electrode delamination. Corresponding glass/ITO-free OPV devices with different numbers of printed grid lines were fabricated. These experiments concluded that 8 lines with a total coverage area of 12.7% provided the optimum inkjet printed silver nanoparticle grid design since

homogeneous charge carrier collection for ITO-free OPVs was established. Devices with the proposed ITO-free electrode configuration delivered repeatable PCE of 2.8% and 4.9% for ITO-free P3HT:PC$_{60}$BM and Si-PCPDTBT:PC$_{70}$BM based OPVs respectively. To our knowledge this is among the highest glass/ITO-free OPV device performance reported in the literature for both materials systems and is achieved by optimizing the sintering processing of the inkjet printed Ag nanoparticles as well as the Ag metal grid design configuration described above. These findings can assist in the future commercialization aspects of OPVs and provide economic attraction towards replacing ITO in a range of other optoelectronic devices applications.

References

[1] F.C. Krebs, Fabrication and processing of polymer solar cells. A review of printing and coating techniques, Sol. Energy Mater. Sol. Cells 93 (2009) 394–412.

[2] H.M. Dong, W.W. Carr, J.F. Morris, Visualization of drop-on-demand inkjet: drop formation and deposition, Rev. Sci. Instrum. 77 (2006) 0851011–0851018.

[3] P.Z. Yin, Y.A. Huang, N.B. Bu, X.M. Wang, Y.L. Xiong, Inkjet printing for flexible electronics: materials, processes and equipments, Chin. Sci. Bull. 55 (2010) 3383–3407.

[4] Z. He, C. Zhong, S. Su, M. Xu, H. Wu, Y. Cao, Enhanced power-conversion efficiency in polymer solar cells using an inverted device structure, Nat. Photon. 6 (2012) 591–595.

[5] J.A. Hauch, P. Schilinsky, S.A. Choulis, R. Childers, M. Biele, C.J. Brabec, Flexible organic P3HT:PCBM bulk-heterojunction modules with more than 1 year outdoor lifetime, Sol. Energy Mater. Sol. Cells 92 (2008) 727–731.

[6] T.Y. Chu, S.W. Tsang, J. Zhou, P.G. Verly, J. Lu, S. Beaupre, M. Leclerc, Y. Tao, High-efficiency inverted solar cells based on a low bandgap polymer with excellent air stability, Sol. Energy Mater. Sol. Cells 96 (2012) 155–159.

[7] H.Y. Chen, J. Hou, S. Zhang, Y. Liang, G. Yang, Y. Yang, L. Yu, Y. Wu, G. Li, Polymer solar cells with enhanced open-circuit voltage and efficiency, Nat. Photon. 3 (2009) 649–653.

[8] S.H. Park, A. Roy, S. Beaupré, S. Cho, N. Coates, J.S. Moon, D. Moses, M. Leclerc, K. Lee, A.J. Heeger, Bulk heterojunction solar cells with internal quantum efficiency approaching 100%, Nat. Photon. 3 (2009) 297–302.

[9] Y. Liang, Z. Xu, J. Xia, S.T. Tsai, Y. Wu, G. Li, C Ray, L. Yu, For the bright future—bulk heterojunction polymer solar cells with power conversion efficiency of 7.4%, Adv. Energy Mater. 22 (2010) 135–138.

[10] C.J.M. Emmott, A. Urbina, J. Nelson, Environmental and economic assessment of ITO-free electrodes for organic solar cells, Sol. Energy Mater. Sol. Cells 97 (2012) 14–21.

[11] B. Azzopardi, C.J.M. Emmott, A. Urbina, F.C. Krebs, Joseph Mutale, Jenny Nelson, Economic assessment of solar electricity production from organic-based photovoltaic modules in a domestic environment, Energy Environ. Sci. 4 (2011) 3741–3753.

[12] N. Grossiord, J.M. Kroon, R. Andriessen, P.W.M. Blom, Degradation mechanisms in organic photovoltaic devices, Org. Electron. 13 (2012) 432–456.

[13] Y. Zhou, H. Cheun, S. Choi, J. William, J. Potscavage, C.F. Hernandez, B. Kippelen, Indium tin oxide-free and metal-free semitransparent organic solar cells, Appl. Phys. Lett. 97 (2010) 153304/1–153304/3.

[14] A. Andersson, N. Johansson, P. Broms, N. Yu, D. Lupo, W.R. Salaneck, Fluorine tin oxide as an alternative to indium tin oxide in polymer LEDs, Adv. Mater. 10 (859) (1998) 859–863.

[15] A.A. Green, M.C. Hersam, Colored semitransparent conductive coatings consisting of monodisperse metallic single-walled carbon nanotubes, Nano Lett. 8 (1417) (2008) 1417–1422.

[16] L.G. de Arco, Y. Zhang, C.W. Schlenker, K. Ryu, M.E. Thompson, C.W. Zhou, Continuous, highly flexible, and transparent graphene films by chemical vapor deposition for organic photovoltaics, ACS Nano 4 (2865) (2010) 2865–2873.

[17] R.R. Søndergaard, M. Hosel, F.C. Krebs, Roll-to-roll fabrication of large area functional organic materials, J. Polym. Sci. Part B Polym. Phys. 51 (2013) 16–34.

[18] M.L. Becker, J.A. Fagan, N.D. Gallant, B.J. Bauer, V. Bajpai, E.K. Hobbie, S.H. Lacerda, K.B. Migler, J.P. Jakupciak, Length-dependent uptake of DNA-wrapped single-walled carbon nanotubes, Adv. Mater. 19 (2007) 939–945.

[19] K.S. Novoselov, V.I. Falko, L. Colombo, P.R. Gellert, M.G. Schwab, K. Kim, A roadmap for graphene, Nature 490 (2012) 192–200.

[20] T. Aernouts, P. Vanlaeke, W. Geens, J. Poortman, P. Heremans, S. Borghs, R. Mertens, R. Andrienssen, L. Leenders, Printable anodes for flexible organic solar cell modules, Thin Solid Films 451 (2004) 22–25.

[21] K. Tvingstedt, O. Inganas, Electrode grids for ITO-free organic photovoltaic devices, Adv. Mater. 19 (2007) 2893–2897.

[22] M.G. Kang, M.S. Kim, J. Kim, L.J. Guo, Organic solar cells using nanoimprinted transparent metal electrodes, Adv. Mater. 20 (2008) 4408–4413.

[23] Y. Galagan, E.W.C. Coenen, S. Sabik, H.H. Gorter, M. Barink, S.C Veenstra, J.M. Kroon, R. Andriessen, P.W.M. Blom, Evaluation of ink-jet printed current collecting grids and busbars for ITO-free organic solar cells, Sol. Energy Mater. Sol. Cells 104 (2012) 32–38.

[24] Y. Galagan, J.E.J.M. Rubingh, R. Andriessen, C.C. Fan, P.W.M. Blom, S.C Veenstra, J.M. Kroon, ITO-free flexible organic solar cells with printed current collecting grids, Sol. Energy Mater. Sol. Cells 95 (2011) 1339–1343.

[25] M. Neophytou, F. Hermerschmidt, A. Savva, E. Georgiou, S.A. Choulis, Highly efficient indium tin oxide-free organic photovoltaics using inkjet-printed silver nanoparticle current collecting grids, Appl. Phys. Lett. 101 (2012) 193302/1–193302/4.

[26] R.D. Deegan, O. Bakajin, T.F. Dupont, G. Huber, S.R. Nagel, T.A. Witten, Capillary flow as the cause of ring stains from dried liquid drops, Nature 389 (1997) 827–829.

[27] H. Hu, R.G. Larson, Marangoni effect reverses coffee-ring depositions, J. Phys. Chem. B 110 (2006) 7090–7094.

[28] David R. Lide, CRC Handbook of Chemistry and Physics, Internet Version, Boca Raton, Florida, 2005.

[29] I. Etxebarria, J.G. Tait, R. Gehlhaar, R. Pacios, D. Cheyns, Surface treatment patterning of organic photovoltaic films for low-cost modules, Org. Electron. 14 (2013) 430–435.

[30] J.H. Yao, K.R. Elder, H. Guo, M. Grant, Theory and simulation of Ostwald ripening, Phys. Rev. B 47 (1993) 14110–14125.

[31] S.I. Na, D.W. Park, S.S. Kim, S.Y. Yang, K. Lee, M.H. Lee, ITO-free flexible polymer solar cells with ink-jet-printed Ag grids, Semicond. Sci. Technol. 27 (2012) 125002–125007.

[32] Y. Galagan, B. Zimmermann, E.W.C. Coenen, M. Jorgensen, D.M. Tanenbaum, F.C. Krebs, H. Gorter, S. Sabik, L.H. Slooff, S.C Veenstra, J.M. Kroon, R. Andriessen, Current collecting grids for ITO-free solar cells, Adv. Energy Mater. 2 (2012) 103–110.

[33] F.C. Krebs, R. Søndergaard, M. Jørgensen, Printed metal back electrodes for R2R fabricated polymer solar cells studied using the LBIC technique, Sol. Energy Mater. Sol. Cells 95 (2011) 1348–1353.

[34] COMSOL, Heat Transfer Module, COMSOL Multiphysics User's Guide, COMSOL AB, Stockholm, Sweden, 2008.

[35] J.D. Servaites, S. Yeganeh, T.J. Marks, M.A. Ratner, Efficiency enhancement in organic photovoltaic cells: consequences of optimizing series resistance, Adv. Funct. Mater. 20 (2010) 97–104.

[36] J.D. Servaites, M.A. Ratner, T.J. Marks, Organic solar cells: a new look at traditional models, Energy Environ. Sci. 4 (2011) 4410–4422.

[37] M. Jørgensen, J.E. Carlé, R.R. Søndergaard, M. Lauritzen, N.A. Dagnæs-Hansen, S.L. Byskov, T.R. Andersen, T.T. Larsen-Olsen, A.P.L. Böttiger, B. Andreasen, L. Fu, L. Zuo, Y. Liu, E. Bundgaard, X. Zhan, H. Chen, F.C. Krebs, The state of organic solar cells—a meta analysis, Sol. Energy Mater. Sol. Cells 119 (2013) 84–93.

[38] J.E. Carlé, F.C. Krebs, Technological status of organic photovoltaics (OPV), Sol. Energy Mater. Sol. Cells 119 (2013) 309–310.